Biophysical Journal
Article

Biophysical Society

The Dimer-of-Trimers Assembly Prevents Catalysis at the Transferase Site of Prokaryotic FAD Synthase

Isaias Lans,[1,2,*] Juan Seco,[1] Ana Serrano,[3] Ricardo Burbano,[1] Pilar Cossio,[2,4] Martha C. Daza,[1] and Milagros Medina[3,*]

[1]Grupo de Bioquímica Teórica, Universidad Industrial de Santander, Bucaramanga, Colombia; [2]Biophysics of Tropical Diseases, Max Planck Tandem Group, University of Antioquia, Medellin, Colombia; [3]Departamento de Bioquímica y Biología Molecular y Celular, Facultad de Ciencias e Instituto de Biocomputación y Física de Sistemas Complejos (Joint Units: BIFI-IQFR and GBsC-CSIC), Universidad de Zaragoza, Zaragoza, Spain; and [4]Department of Theoretical Biophysics, Max Planck Institute of Biophysics, Frankfurt am Main, Germany

ABSTRACT Flavin mononucleotide (FMN) and flavin-adenine dinucleotide (FAD) are essential flavoprotein cofactors. A riboflavin kinase (RFK) activity catalyzes riboflavin phosphorylation to FMN, which can then be transformed into FAD by an FMN:adenylyltransferase (FMNAT) activity. Two enzymes are responsible for each one of these activities in eukaryotes, whereas prokaryotes have a single bifunctional enzyme, FAD synthase (FADS). FADS folds in two independent modules: the C-terminal with RFK activity and the N-terminal with FMNAT activity. Differences in structure and chemistry for the FMNAT catalysis among prokaryotic and eukaryotic enzymes pointed to the FMNAT activity of prokaryotic FADS as a potential antimicrobial target, making the structural model of the bacterial FMNAT module in complex with substrates relevant to understand the FADS catalytic mechanism and to the discovery of antimicrobial drugs. However, such a crystallographic complex remains elusive. Here, we have used molecular docking and molecular dynamics simulations to generate energetically stable interactions of the FMNAT module of FADS from *Corynebacterium ammoniagenes* with ATP/Mg^{2+} and FMN in both the monomeric and dimer-of-trimers assemblies reported for this protein. For the monomer, we have identified the residues that accommodate the reactive phosphates in a conformation compatible with catalysis. Interestingly, for the dimer-of-trimers conformation, we have found that the RFK module negatively influences FMN binding at the interacting FMNAT module. These results agree with calorimetric data of purified samples containing nearly 100% monomer or nearly 100% dimer-of-trimers, indicating that FMN binds to the monomer but not to the dimer-of-trimers. Such observations support regulation of flavin homeostasis by quaternary *C. ammoniagenes* FADS assemblies.

INTRODUCTION

Flavoenzymes and flavoproteins use as cofactors flavin mononucleotide (FMN) and flavin-adenine dinucleotide (FAD), which in organisms from all kingdoms are synthetized from the riboflavin precursor (RF, vitamin B2). Transformation of RF into FMN is catalyzed by a riboflavin kinase activity (RFK, Enzyme Commission 2.7.1.26). Then, an ATP:FMN:adenylyltransferase activity (FMNAT, Enzyme Commission 2.7.7.2) converts FMN into FAD (1–3). Both activities use as a second substrate ATP:Mg^{2+} and produce as a coproduct ADP and pyrophosphate, respectively. Interestingly, these two activities reside in two different enzymes in eukaryotes, but in most prokaryotes, they are contained in a single bifunctional and bimodular enzyme known as FAD synthase (FADS). In these bifunctional enzymes, the RFK activity occurs at the protein C-terminal module (RFK module) (4,5), whereas the FMNAT activity is catalyzed at the N-terminal module (FMNAT module) (5,6). Because the FMNAT module lacks both sequence and structural homology with eukaryotic FMNATs, prokaryotic FADSs have emerged as potential antimicrobial targets (5,7–9).

The FADS from *Corynebacterium ammoniagenes* (*Ca*FADS) is so far the best characterized member of the family, and it is considered a good model for the FADS from the human pathogen *Mycobacterium tuberculosis* (8,9). *Ca*FADS crystallographic structures are available for the full-length protein free of ligands (apo form), as well as for the RFK module in complex with adenine and flavin nucleotide ligands (holo form) (5,10). Even though no experimental structures of the FMNAT module in complex with substrates have been reported up to now (Fig. 1), models based on other nucleotidyltransferases have been produced to tentatively allocate ATP/Mg^{2+} and

Submitted April 13, 2018, and accepted for publication August 13, 2018.

*Correspondence: grupobiotd.posdoc@udea.edu.co or mmedina@unizar.es

Editor: Monika Fuxreiter.

https://doi.org/10.1016/j.bpj.2018.08.011

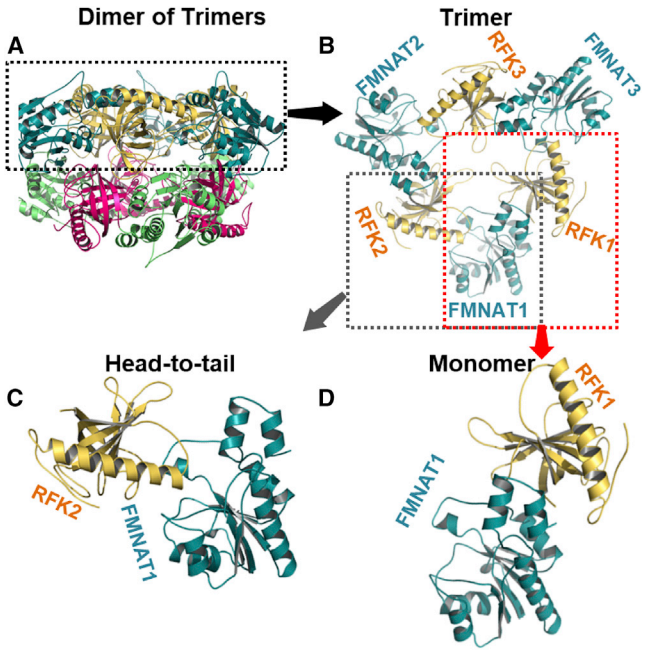

FIGURE 1 The structure of the apo form of *Ca*FADS (PDB: 2X0K). (*A*) A lateral view of the dimer-of-trimers organization predicted by the PDBePISA server is shown. The top and bottom trimers are colored in yellow-blue (RFK-FMNAT modules) and pink-green (RFK-FMNAT modules), respectively. (*B*) A top view of one of the trimers, showing the three protomers in the apo head-to-tail organization among the FMNAT (*blue*) and RFK (*yellow*) modules of contiguous protomers, is shown. (*C*) Details of the head-to-tail organization between FMNAT1 module (*blue*) and RFK2 module (*yellow*) of contiguous protomers are shown. (*D*) A cartoon model of a *Ca*FADS monomer distinguishing its FMNAT1 (*blue*) and RFK1 (*yellow*) modules is shown. To see this figure in color, go online.

FMN at the FMNAT module (5). However, these models are not energetically optimized and therefore might not show a realistic position of the atoms involved in catalysis. In addition, by exploring macromolecular interfaces and symmetry in the apo *Ca*FADS X-ray crystallographic structure, a dimer-of-trimers assembly (Fig. 1 *A*) was predicted to be stable in solution (5). Formation of such assemblies was also imaged at the single-molecule level along with catalysis and detected in vivo (11). Within each trimer, the FMNAT module of one protomer approaches the RFK module of the neighboring protomer (Fig. 1 *B*), and the active sites of the RFK and FMNAT modules can be in close contact with a head-to-tail configuration (5) (Fig. 1 *C*). Enzymatic systems can use oligomeric assemblies to regulate activity (12), and this might be the case with *Ca*FADS. In this context, site-directed mutagenesis has proven that particular mutations at one *Ca*FADS module can modulate the activity of the other module, with the dimer-of-trimers organization as a possible candidate to generate these effects (6,13,14). However, for the moment, it is not understood how the interplay between the FMNAT and RFK domains exerts this modulation.

Here, we use docking and molecular dynamics (MD) simulations to produce energetically optimized models that elucidate the interaction of the *Ca*FADS FMNAT module with its substrates, ATP/Mg^{2+} and FMN. The models have been produced considering both the single FMNAT module as well as the FMNAT:RFK head-to-tail organization found in each trimer of the dimer-of-trimers (Fig. 1). Docking of substrates to the FMNAT module produced a model that allows visualizing how several residues, experimentally proposed as key in binding and catalysis, contribute to substrates binding. In particular, our MD simulations show accommodation of the reactive phosphate groups of ATP and FMN in a conformation compatible with catalysis. In addition, the results suggest that in the head-to-tail configuration, the RFK module might impair FMN binding at the FMNAT active site and as a consequence the approaching of the reactive donor and acceptor atoms.

MATERIALS AND METHODS

Molecular docking

The Cartesian coordinates of the FMNAT module (M1-H186) of *Ca*FADS were taken from the PDB structure 2X0K and used as receptor for the docking (5). Autodock4.2 (15–17) was used to obtain the initial interaction models of the FMNAT module with its substrates, ATP/Mg^{2+} and FMN. The space sampling was defined using a grid box of 60 points in each dimension. To obtain better precision for the Mg^{2+} position, we used a grid spacing of 0.25 Å. The search was performed using the Lamarckian genetic algorithm implemented in Autodock with a starting population of 150 individuals, using 25,000,000 energy evaluations and 27,000 generations. The resultant poses were clustered using the root mean-square deviation (RMSD) of the atomic positions, with a tolerance of 2.0 Å, and the Autodock default cluster method.

Docking of ATP/Mg^{2+} and FMN to the FMNAT module

Models for the simultaneous interaction of substrates with the receptor were obtained in three steps: 1) first, we obtained the ATP interaction model, using as grid box center the OD1 atom of the N125 side chain; 2) then, we used the obtained FMNAT:ATP model as receptor to dock Mg^{2+} and produced the FMNAT:ATP/Mg^{2+} model, using the Pβ of ATP as the grid box center; 3) finally, we used this FMNAT:ATP/Mg^{2+} model as receptor to produce the holo-FMNAT interaction model, using in this case the α-carbon of T127 as the grid box center. The docking zones were chosen based on the available protein-ligand complexes of homologous enzymes. We used the AMP-FADS from *Thermotoga maritima* (1T6Y) and the NAD^+ nicotinamide-mononucleotide-adenylyl-transferase from *Methanobacterium thermoautotrophicum* (1EJ2) (18) complexes to choose the ATP and FMN docking zones, respectively.

Docking of FMN to the FADS:ATP/Mg^{2+} complex within the FMNAT:RFK head-to-tail organization

We aligned the FMNAT:ATP/Mg^{2+} interaction model (from the previous docking procedure) onto the FMNAT module of a protomer of the *Ca*FADS dimer-of-trimers (e.g., FMNAT1 in Fig. 1 *B*) and built a head-to-tail FMNAT:ATP/Mg^{2+}:RFK model by incorporating the coordinates of the RFK module (F187–S338) of the neighboring protomer interfacing the

FMNAT:ATP/Mg^{2+} complex (e.g., RFK2 in Fig. 1 *B*). This provided us with a head-to-tail FMNAT:ATP/Mg^{2+}:RFK model that was then used as receptor to dock FMN and to obtain a holo head-to-tail model. The α-carbon of T127 was used as the grid box center.

MD simulations

Molecular docking complexes were prepared for MD simulations using the charmm-gui webserver (19,20). The PROPKA (21) module of the PDB2PQR software package (22,23) was used to determine the protonation state of all ionizable groups at pH 7.0. Complexes were protonated using the HBUILD tool. The final models were solvated with a previously equilibrated cubic box of water molecules centered at the geometric center of the complex. To neutralize the FMNAT:ATP/Mg^{2+}:FMN and FMNAT:ATP/Mg^{2+}:FMN:RFK systems, 13 and 24 K^+ ions, respectively, were added as counterions. The final systems contained 32,226 and 80,856 atoms, respectively. The charmm36 force field (24–27) was used to model the system with a transferable intermolecular potential with 3 points water model. ATP and FMN force-field parameters were taken from Pavelites et al. (28) and Freddolino et al. (29), respectively. Both systems were minimized until the maximal force was <1000 kJ/mol • nm by using the steepest descent algorithm.

MD simulations were carried out with periodic boundary conditions. A spherical cutoff of 1.2 nm for the nonbonded interactions was applied together with a switch function acting between 1.0 and 1.2 nm. The nonbonded pair list was updated every 20 steps. The particle mesh Ewald method was used to compute long-range electrostatic force terms and the leapfrog algorithm to propagate the equations of motion. All bond lengths and angles involving hydrogen atoms were constrained by the LINCS algorithm (30). Equilibration consisted of 25 ps of NVT (constant number of particles, volume, and temperature) simulation at 300.15 K, with a time step of 1 fs. During equilibration, the coordinates of the protein backbone and of the ligand heavy atoms were restrained using a constant force of 400 kJ/mol • nm while protein side chains were restrained using a constant force of 40 kJ/mol • nm. Finally, MD simulations of 200 ns were carried out using the Gromacs 5.1.3 program (19,31,32) with a time step of 2 fs, without restraints, in an isothermal-isobaric (NPT) ensemble at 300.15 K and 1 atm. Three replicas were done for each model. We carried out the following MD simulations: 1) three replicas of the holo head-to-tail configuration, using as starting structures three poses from the docking cluster with lower score. One starting structure was the configuration with overall lowest score, and the other two were random poses from the same docking cluster. Pseudorandom velocities were generated according to a Maxwell distribution at 300.15 K; 2) three replicas of the apo head-to-tail configuration (Fig. 1 *C*), using as a starting structure the dimer-of-trimers assembly predicted from the crystallographic structure with pseudorandom initial velocities generated according to a Maxwell distribution at 300.15 K; 3) three replicas of the monomeric holo-FMNAT complex, using as starting structures three poses from the docking cluster with lower scores. One starting structure was the configuration with overall lowest score, and the other two were random poses from the same docking cluster. Pseudorandom velocities were generated according to a Maxwell distribution at 300.15 K.

Purification of samples of monomeric and oligomeric *Ca*FADS and determination of their flavin-binding ability

*Ca*FADS was overexpressed in BL21(DE3) *Escherichia coli* cells using the pET28a-*Ca*FADS plasmid and purified after 20% ammonium sulfate fractionation, followed by sequential phenyl-sepharose and diethylethanolamine-cellulose chromatographic steps as previously reported (5,6). Monomeric and oligomeric fractions were quantitatively separated by gel filtration with a HiPrep 26/60 Sephacryl S-200 High Resolution column (GE Healthcare, Chicago, IL) as reported elsewhere (6,11). Binding affinities of flavin ligands to such freshly separated monomeric and oligomeric samples were evaluated by isothermal titration calorimetry (ITC) using a high precision VP-ITC calorimeter (MicroCal LLC, Northampton, MA) with the thermostat set at 25°C. Interaction parameters were obtained by direct titration of *Ca*FADS ($\sim$20 μM in the cell) with RF, FMN, or FAD ($\sim$200 μM in the syringe) in 20 mM 1,4-piperazinediethanesulfonic acid, 10 mM $MgCl_2$ (pH 7.0), following the procedures described previously (13,33,34). A home-derived model for one or two independent binding sites implemented in Origin 7.0 (OriginLab Corporation, Northampton, MA) was used to determine the binding stoichiometry (N) and thermodynamic parameters (33,34).

RESULTS AND DISCUSSION

ATP and FMN substrates bind to the FMNAT module in a reactive conformation

Former kinetic characterization of the FMNAT activity of *Ca*FADS indicated an ordered mechanism of catalysis in which ATP binds before FMN (35). Therefore, we followed such binding order to produce our substrates-bound docking model. After docking of ATP into the FMNAT module, we chose the FMNAT:ATP interaction model among poses of cluster 1 (Table 1). This is the largest cluster, according to the Autodock4.2 scoring function, and has an average score 2.3 kcal/mol lower than the next cluster. Cluster 1 has ATP interacting with residues highly conserved in prokaryotic FADSs and previously demonstrated as relevant for ATP binding (5,7,8,33). The difference in the poses from this cluster is small, as given by the average RMSD of 0.48 $\pm$ 0.26 Å. We selected as the representative structure a pose that orients the ATP α-phosphate (Pα) toward the predicted FMN binding site, with the adenine moiety of ATP bound to a cavity formed by H28, H31, and L154 and H-bonded to the L155 and I162 backbone atoms (Fig. S1 *A*). Such binding is similar to that of the AMP competitive inhibitor in the crystallographic structure of *T. maritima* FADS (PDB: 1T6Y) (36) and to that predicted when sculpting the ATP at the FMNAT module of *Ca*FADS based on such a binary complex (5). The ATP ribose moiety sits in a cavity formed by the F24, N125, and F126 side chains and H-bonds to G123 (Fig. S1 *B*). The S164 and R168 side chains stabilize the ATP β- and γ-phosphates (Pβ and Pγ), whereas Pα and Pβ adopt a conformation similar to that of pyrophosphate in the *Ca*FADS crystallographic structure (PDB: 2X0K) (Fig. S1, *C* and *D*). In addition, docking of Mg^{2+}

TABLE 1 Analysis of ATP Docking to the *Ca*FADS FMNAT Module

Cluster[a]	Best Score [kcal/mol]	Mean Cluster Score [kcal/mol]	Number of Poses
1	−11.05	−9.48 ± 0.92	71
2	−7.88	−7.13 ± 0.64	10
3	−7.75	−7.62 ± 0.14	2
4	−7.49	−7.07 ± 0.43	2
5	−7.66	−7.20 ± 0.36	2

[a]First five populated clusters.

(see Materials and Methods) to the chosen FMNAT:ATP interaction model predicts a unique position for the cation that is coordinated by the oxygen atoms of the three ATP phosphates (Fig. S1 *C*).

We then used this FMNAT:ATP/Mg^{2+} model as receptor to dock FMN to obtain a ternary complex model that contains both substrates of the FMNAT activity. Binding scores for the best two clusters were similar (−8.6 and −7.9 kcal/mol) (Table 2). Both clusters showed a similar FMN binding conformation, but they differed in flavin ring orientation (Fig. S2). The most energetically favorable orientation shows the methyls of the isoalloxazine ring oriented toward the solvent (herein named FMN-ME). In the other, the flavin ring flips 180° and its methyls get buried at the bottom of the isoalloxazine binding site (FMN-MB). In both poses, the FMN phosphate (P-FMN) coordinates to the Mg^{2+} cation and situates next to Pα, enabling the possibility of the adenylyl transfer to occur. The isoalloxazine ring sits in a hydrophobic pocket (formed by F54, P58, Y106, and F128) and Π-stacks to F62 (Fig. S2) in a chemical environment typical for the flavin ring in flavoproteins (37,38). Independently of the isoalloxazine orientation, T127 H-bonds to the FMN ribityl hydroxyls, bringing the cofactor phosphate towards Pα (Fig. S2). Therefore, both of our FMNAT:ATP/Mg^{2+}:FMN (henceforth holo-FMNAT) ternary models may favor the occurrence of the adenylylation reaction. We carried out three replicas of MD simulations to study the stability of this docking complex. Because the FMN-ME orientation is usual in flavoproteins (37–39) and belongs to the most populated cluster, we chose three poses from this cluster as staring MD structures. The first one was the configuration with the overall lowest score, and the other two were random poses from the same docking cluster. To evaluate equilibrium stability, we simulated 200 ns of MD for each starting structure. By monitoring the heavy atoms' RMSD, we find that the system reached equilibrium at around 10 ns of simulation (Fig. S3 *A*), and the ATP/Mg^{2+} and FMN ligands kept their binding sites until the end of the simulation (Fig. 2). The MD simulations showed the stabilization of the negative charges of the ATP phosphates by the N-terminal of the α6n helix (163-SSTTVR-168), specifically residues S163, S164, T165, and R168 (Fig. 2, *A* and *B*), whereas the Mg^{2+} ion coordination remained stable (Fig. S3 *B*). The simulations show that residues H31 and N125

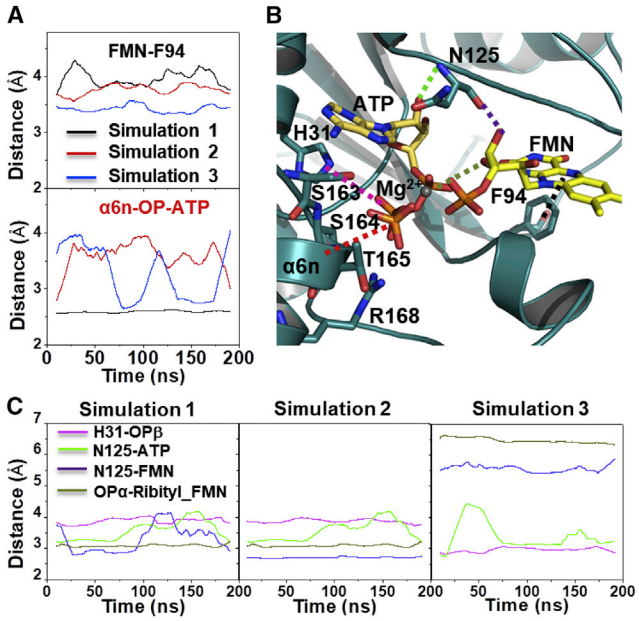

FIGURE 2 Trajectories and snapshot of selected interaction distances along the three MD simulation replicas of the holo-FMNAT model. (*A*) The time window average (using a 20 ns window) of the minimal heavy atom distances between the flavinic ring and F94 (*upper panel*) and of potential H-bonds or electrostatic bridges between the N-terminal of α6n helix and the ATP phosphates (*bottom panel*) is shown. (*B*) A snapshot at 150 ns of one of the MD simulations is shown, highlighting positions and distances considered in the trajectory panels. (*C*) The time window average (using a 20 ns window) of the minimal distance H-bond donor/acceptor pairs is shown: H31-ATP, N125-ATP, N125-FMN, and Pα oxygens-ribityl of FMN (*magenta*, *green*, *violet*, and *olive*, respectively). The H31 and N125 residues contribute to the ATP-FMN orientation. To see this figure in color, go online.

contribute to the orientation of the substrates in the FMNAT adenylylation site (Fig. 2 *C*). The MD trajectories for the three starting poses (Fig. S4) kept contacts between H31 and the ATP phosphates (*magenta lines* in Fig. 2 *C*). In two of the simulations, the N125 spontaneously contributed to stabilize the position of both substrates (*green* and *violet lines*, respectively, in Fig. 2 *C* simulation 1 and 2), maintaining the reactant atoms in close distance. However, in the third simulation, the interaction of N125 with FMN is not spontaneously formed, and as a consequence, the reactant atoms separate (Fig. 2 *C*, simulation 3). Thus, H31 and N125 appear to strongly influence the ATP position, and N125 works as a

TABLE 2 Analysis of FMN Docking to the *Ca*FADS FMNAT:ATP/Mg^{2+} Model

Cluster	Best Score [kcal/mol]	Mean Cluster Score [kcal/mol]	Number of Poses	FMN Binding [a]	Pα-ATP/P-FMN Distance (Å)
1	−8.62	−7.66 ± 0.38	65	FMN-ME	4.5
2	−7.92	−7.00 ± 0.41	19	FMN-MB	4.9
3	−6.60	−6.37 ± 0.19	12	FMN-MB	5.0
4	−7.13	−7.07 ± 0.05	3	FMN-MB	5.3
5	−6.42	−6.42	1	FMN-ME	4.6

[a]Clusters show two FMN binding orientations: the FMN isoalloxazine methyls are either exposed toward the solvent (FMN-ME) or buried at the bottom of the flavin binding pocket (FMN-MB).

link to approach the reactant atoms (*olive lines* Fig. 2 *C*, simulation 1 and 2). Altogether, our holo-FMNAT docking complex and MD simulation analyses predict key roles for H31 and the N-terminal α6n helix (S163–T165 and R168) in the catalytically competent binding of ATP, as well as for N125 as the catalytic base in the FMNAT activity, in agreement with former mutational studies (6,34).

The head-to-tail conformation reduces the affinity of the FMNAT site for the FMN substrate

In the holo-FMNAT ternary complex presented above, a large portion of the FMN molecule is exposed to the solvent. However, when considering the head-to-tail trimers (Fig. 1 *B*), FMN would sit at the FMNAT module area interfacing with the RFK module of the neighboring protomer. Therefore, formation of trimers might influence FMN binding. To evaluate such a possibility, we built a receptor that incorporates the coordinates of the RFK module of the neighboring head-to-tail protomer to the FMNAT:ATP/Mg^{2+} model (Fig. 1 *C*) and docked FMN on the resulting structure. Docking results predicted very low FMN binding affinity (Table 3), particularly when compared to those in which the RFK module is absent (Table 2). Such observation points to the predicted apo *Ca*FADS dimer-of-trimers being considerably less prone to bind FMN compared to the protein monomer. All clusters with negative mean binding energy show binding of the isoalloxazine ring with methyls in the ME conformation (Fig. S5; Table 3), in agreement with this conformation being favorable in multimeric flavoprotein arrangements (36–38). For the best pose, cluster 1, the isoalloxazine sits in a hydrophobic pocket with its C2 carbonyl H-bonded to the Y106 side chain while the FMN ribityl would also H-bond to T127 (Fig. S5). However, the positions of the ribityl end and the P-FMN are now also influenced by residues of the interacting RFK module, particularly by S299 and V300, situated at loop L6c and helix α1c, respectively (Fig. S5). In agreement with our results, former mutational data pointed to these residues as modulators of the geometry of quaternary assemblies as well as of the substrates' binding affinity and of the kinetic parameters of both the RFK and FMNAT activities (13).

We used MD simulations to evaluate the stability of the FMNAT:ATP/Mg^{2+}:FMN-ME:RFK (hereinafter holo head-to-tail) complex obtained from the docking calculations. We performed three MD simulations, starting from different poses belonging to the docking cluster with lowest score. These simulations show considerable fluctuations and changes in the RMSD of the entire complex (*black lines* in the *upper panels* of Fig. 3). However, the RMSD of the individual FMNAT and RFK modules are stable (*red* and *blue lines* in Fig. 3, *upper panels*). The high overall RMSD fluctuation mostly relates to the pivoting of the RFK module over the FMNAT module (*bottom panels* in Fig. 3; Fig. S6). In all the holo head-to-tail simulations, we observe reorientation or semidissociation of the RFK module in relation to the FMNAT module (Fig. S6). These results validate the hypothesis that positioning of the substrate in the FMNAT cavity requires changes in the relative disposition of the RFK and FMNAT modules regarding the head-to-tail assembly found in the predicted apo dimer-of-trimers (10).

Additional evidence of the negative effect of the head-to-tail configuration on the binding of the substrates are found in the three MD simulations of 200 ns of the head-to-tail conformation without the substrates (apo head to tail). As shown by the RMSD of the entire complex (Fig. S7), we find that the apo head-to-tail configuration does not present as large reorientations or fluctuations between the RFK and FMNAT modules as in the corresponding model with the substrates. On the contrary, in this case, residue D298 of the RFK L1c loop fills the FMNAT ligand binding site (Fig. 4). These results support the idea that the head-to-tail configuration reduces the probabilities for the binding of FMN at the FMNAT active site.

Even though the substrate-positioning in the FMNAT site requires changes in the relative disposition of the RFK and FMNAT modules, the MD simulations of the holo head-to-tail complex show some interactions that simultaneously contribute to its stabilization and impair, directly or indirectly, the stable placement of the substrates in a catalytically favorable configuration. This is the case with the head-to-tail R66/R65(FMNAT):E268(RFK) salt bridge and the V300(RFK) van der Waals contact with methyls of the FMN isoalloxazine (*bottom panels* in Fig. 3). This agrees with R66 substitutions impairing the RFK turnover as well as modulating the monomer/oligomer ratios and the conformation of quaternary arrangements (6). Therefore, computational and mutational data support the mutual activity-modulation hypothesis between

TABLE 3 Analysis of FMN Docking to the *Ca*FADS FMNAT:ATP/Mg^{2+}:RFK Model

Cluster	Best Score [kcal/mol]	Mean Cluster Score [kcal/mol]	Number of Poses	FMN Binding[a]	Pα-ATP/P-FMN Distance (Å)
1	−2.47	−0.99 ± 0.49	65	FMN-ME	5.3
2	−0.23	0.21 ± 0.33	19	FMN-MB	12.8
3	−0.44	0.18 ± 0.48	8	FMN-MB	16.8
4	0.04	0.58 ± 0.65	4	FMN-MB	5.2
5	−1.1	−0.89 ± 0.21	2	FMN-ME	7.2

[a]Clusters show two FMN binding orientations: the FMN isoalloxazine methyls are either exposed toward the solvent (FMN-ME) or buried at the bottom of the flavin binding pocket (FMN-MB).

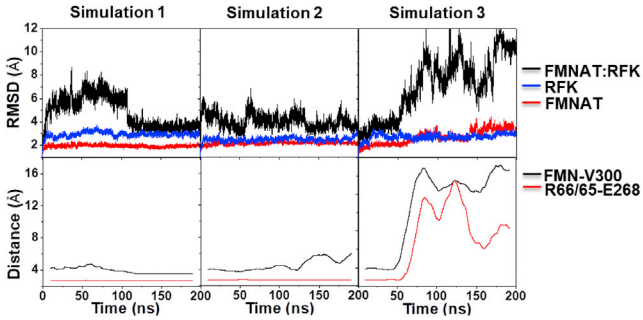

FIGURE 3 Relative disposition of RFK and FMNAT modules along three MD simulations replicas of the holo head-to-tail complex. The upper panels show the RMSD trajectories when considering only the FMNAT (*red line*) or RFK (*blue line*) modules and when considering the overall structure (*black line*). The RMSD values are calculated relative to the starting MD structure. Profiles show reorientation and even semidissociation of the RFK module in relation to the FMNAT module. Bottom panels show evolution of the FMN-V300 (RFK) and R66/R65 (FMNAT)-E268 (RFK) minimal distances (*black* and *red lines*, respectively), indicating a change in the head-to-tail interphase. To see this figure in color, go online.

the RFK and FMNAT modules of neighboring protomers in *Ca*FADS.

The results from the MD simulations also show that the RFK module induces a change in the interaction profile of the FMNAT module with its ligands, ATP and FMN, with the holo head-to-tail model showing a deeper location of the ATP substrate in the binding cavity (*magenta lines* in Fig. S8). In these simulations, the N125 catalytic base shows a tendency to lose contacts with the FMN ribityl (*violet lines* in Fig. S8), and the distance between the FMN and ATP ligands increases (*olive lines* in Fig. S8). These observations point to the idea that the head-to-tail configuration and the

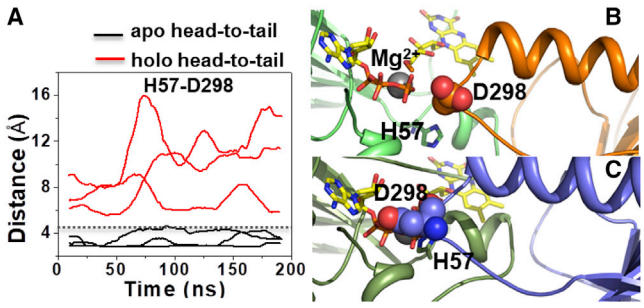

FIGURE 4 (*A*) Trajectories of potential H-bonds between H57 (FMNAT) and D298 (RFK) along the MD simulations of the apo head-to-tail (*black lines*) and holo head-to-tail (*red lines*) models. The apo head-to-tail configuration shows shorter H57-D298 distances than the corresponding distances in either the crystallographic (*dotted line*) or holo head-to-tail complexes. (*B*) A snapshot of the holo head-to-tail configuration at 150 ns of MD simulations is shown. Ligands, FMNAT, and RFK modules are shown in yellow, green, and orange, respectively. Residues H57 and D298 are shown in sticks and balls, respectively. (*C*) A snapshot of the apo head-to-tail configuration at 150 ns of MD simulations is shown. The RFK module (*light blue*) fills part of the FMNAT (*olive*) active site. The ligands (*yellow*) in (*C*) are shown for illustrative reasons (these ligands correspond to those in (*B*)). To see this figure in color, go online.

lack of simultaneous N125-ATP and N125-FMN interactions contribute to reduce competent FMN binding.

The *Ca*FADS dimer-of-trimers is a plausible cell strategy to control flavin cofactor production and delivery

Here, we have presented energetically stable models for the simultaneous binding of the ATP/Mg^{2+} and FMN substrates to the FMNAT active site of *Ca*FADS. These models correspond to the theoretical binding of substrates when the protein behaves as a monomer or when it is part of the dimer-of-trimers assembly. The binding model in the monomeric protein sits the reacting atoms for the adenylylphosphate group transfer from ATP to the P-FMN at an adequate distance and orientation, allowing FAD production. In addition, it agrees with former mutational analyses in residues involved in substrates' location at their binding pocket (6,34). Moreover, this model shows N125 linking the Pα donor to the terminal end of the ribityl acceptor (Fig. 2 *C*), in line with its formerly proposed role as catalytic base for the FMNAT reaction (34).

Our predicted head-to-tail docking model shows how the RFK module of the neighboring protomer influences the interaction of FMNAT residues, including the N125 catalytic base, with the ATP and FMN substrates. Moreover, it is remarkable the low FMN binding affinity at the FMNAT active site predicted in this docking (Table 3). Also notable are the effects of the presence of ligands in the overall RMSD changes in the head-to-tail MD simulations that indicate deleterious effects in the protomer-protomer interaction. Moreover, this model also increases the relative distance between substrates compared to the monomeric model (*olive lines* in Figs. 2 and S8). Such inferences are in line with former experimental kinetic data for the *Ca*FADS FMNAT activity (5). Those studies showed samples enriched in the dimer-of-trimers assembly having a sevenfold lower turnover than the monomer, whereas its K_m^{FMN} increased by ~6-fold (5). Thus, the dimer-of-trimers assembly would only retain 2% of the monomeric *Ca*FADS efficiency, and the reason for this low efficiency might be the reduced affinity for the FMN substrate at the FMNAT site in the dimer-of-trimers assembly.

To prove such a deleterious effect in FMN binding, here we have used ITC to experimentally evaluate the Gibbs binding energy for the interaction of free flavins with samples containing freshly separated (just before measurement) *Ca*FADS monomer and dimer-of-trimers (Fig. S9). Former studies indicated that on samples estimated as more than 95% monomer (but not freshly separated monomer), in the absence of adenine nucleotides, RF can bind at both RFK and FMNAT modules, whereas FMN and FAD would only bind at the FMNAT module (33). In agreement with this, thermograms for the titration of our freshly purified monomer (Fig. S9, *A–C*) are indicative of the binding of

two RF molecules and just one FMN or FAD molecules per monomer. On the contrary, when titrating the freshly purified *Ca*FADS dimer-of-trimers with either FMN or FAD, no heat exchange was detected (Fig. S9, *E* and *F*), indicating a lack of favorable enthalpic contributions to the binding. These results agree with the fact that the presence of the RFK module of a neighboring protomer abolishes specific protein-ligand interactions that impair the flavin location at the FMNAT binding cavity. Moreover, RF only binds to a single site of each protomer (Fig. S9 *D*) that, as previously indicated (33), must be at the RFK module. Therefore, the low FMNAT efficiency previously reported for the dimer-of-trimers assembly appears as a consequence of the presence of the RFK module of the neighboring protomer within each trimer blocking FMN access to the FMNAT binding site. Previous in vitro mutational studies already pointed to a modulator effect of RFK module residues (such as P208, T210, E268, and V300) on the FMNAT activity and ligands' affinity, as well as to mutations in the FMNAT module with impact on the RFK activity (6,13,14,34). In this context, it is worth noting that mutations preventing the head-to-tail R66/R65(FMNAT):E268(RFK) salt bridge enhance the FMNAT catalytic efficiency (6,14). Therefore, the model presented here provides us with clues about which residues of the RFK module contribute to both the head-to-tail assembly and the FMNAT activity modulation. Particularly, it helps us to understand why 1) formation of the strong R66/R65(FMNAT):E268(RFK) salt bridge indirectly modulates the shape of the P-FMN binding site and 2) V300 influences the FMN ribityl orientation. Both facts might contribute to impair the interaction of the reaction acceptor atom with the N125 catalytic base as well as to increase the distance between the ligands. It is also important to consider that changes described in the RFK module loops during its catalytic activity (10,40) have a clear impact on the FMNAT substrates' binding site, particularly affecting L3n (residues 55–57), α3n (58–62), and L4n (63–73) (see Fig. 10 in Herguedas et al. (10)). Thus, as envisaged from our MD simulations, the RFK module would require pivoting to adapt its interaction surface to the FMNAT module when its ligands are bound (Figs. S7 and S9).

To date, the function of the monomer-oligomer equilibrium in *Ca*FADS is not yet clear. However, the experimental and simulation results from this study indicate that such quaternary organization is less prone to bind flavinic substrates at the FMNAT site, and as a consequence, the head-to-tail organization is less efficient for FAD production. Thus, the head-to-tail conformation could be a mechanism to reduce the *Ca*FADS affinity for FMN at the FMNAT site. From previous studies, we know that monomer and oligomer *Ca*FADS exists in equilibrium in solution (11). Therefore, *Ca*FADS oligomerization could be able to modulate the equilibrium between flavinic compounds (FMN/FAD) and hence the flavin homeostasis.

In conclusion, in the absence of experimental structures showing substrate binding to the FMNAT active site, the holo-FMNAT model here presented provides a good structure of the putative binding of substrates during the *Ca*FADS FMNAT activity, showing the contribution of H31, R66, N125, S163, S164, T165, and R168 to the formation of a catalytically competent complex for the adenylylation of FMN. In addition, the results from the simulations for the dimer-of-trimers assembly show that the presence of the RFK module (particularly residues E268, D298, and V300) considerably impairs FMN binding at the FMNAT active site of *Ca*FADS and as a consequence decreases the FMNAT catalytic efficiency.

SUPPORTING MATERIAL

Nine figures are available at http://www.biophysj.org/biophysj/supplemental/S0006-3495(18)30963-9.

AUTHOR CONTRIBUTIONS

I.L. designed and performed research, interpreted data, and wrote the manuscript. J.S. performed research and interpreted data. A.S. designed and performed ITC research and interpreted data. R.B. performed research. M.C.D. designed research and interpreted data. P.C. interpreted data and wrote the manuscript. M.M. designed research, interpreted data, and wrote the manuscript. All authors read and approved the final version.

ACKNOWLEDGMENTS

This work has been supported by Departamento Administrativo de Ciencia, Tecnología e Innovación (Colciencias, programa "Es tiempo de volver" and "Max Planck agreement"), Vicerrectoría de Investigación y Extensión Universidad Industrial de Santander (project 1818 to M.C.D), University of Antioquia (Colombia), the Max Planck Society (Germany), the Spanish Ministry of Economy, Industry and Competitiveness (BIO2016-75183-P AEI/FEDER, UE to M.M.) and the Government of Aragón-Fondo Europeo de Desarrollo Regional (E35_17R). Computations were performed on the Apolo cluster, Eafit University (Colombia), and on two Dell PowerEdge T630 servers, one with a NVIDIA graphics processing unit. P.C. gratefully acknowledges NVIDIA for the donation of this graphics processing unit.

REFERENCES

1. Fischer, M., A. Bacher, and J. Pero. 2005. Biosynthesis of flavocoenzymes. *Nat. Prod. Rep.* 22:324–350.
2. Barile, M., C. Brizio, …, S. Passarella. 2000. The riboflavin/FAD cycle in rat liver mitochondria. *Eur. J. Biochem.* 267:4888–4900.
3. Bafunno, V., T. A. Giancaspero, …, M. Barile. 2004. Riboflavin uptake and FAD synthesis in Saccharomyces cerevisiae mitochondria: involvement of the Flx1p carrier in FAD export. *J. Biol. Chem.* 279:95–102.
4. Serrano, A., P. Ferreira, …, M. Medina. 2013. The prokaryotic FAD synthetase family: a potential drug target. *Curr. Pharm. Des.* 19:2637–2648.
5. Herguedas, B., M. Martínez-Júlvez, …, J. A. Hermoso. 2010. Oligomeric state in the crystal structure of modular FAD synthetase provides insights into its sequential catalysis in prokaryotes. *J. Mol. Biol.* 400:218–230.

6. Serrano, A., M. Sebastián, …, M. Medina. 2015. Quaternary organization in a bifunctional prokaryotic FAD synthetase: involvement of an arginine at its adenylyltransferase module on the riboflavin kinase activity. *Biochim. Biophys. Acta.* 1854:897–906.
7. Krupa, A., K. Sandhya, …, S. Jonnalagadda. 2003. A conserved domain in prokaryotic bifunctional FAD synthetases can potentially catalyze nucleotide transfer. *Trends Biochem. Sci.* 28:9–12.
8. Frago, S., M. Martínez-Júlvez, …, M. Medina. 2008. Structural analysis of FAD synthetase from Corynebacterium ammoniagenes. *BMC Microbiol.* 8:160.
9. Sebastián, M., E. Anoz-Carbonell, …, M. Medina. 2018. Discovery of antimicrobial compounds targeting bacterial type FAD synthetases. *J. Enzyme Inhib. Med. Chem.* 33:241–254.
10. Herguedas, B., I. Lans, …, M. Medina. 2015. Structural insights into the synthesis of FMN in prokaryotic organisms. *Acta Crystallogr. D Biol. Crystallogr.* 71:2526–2542.
11. Marcuello, C., S. Arilla-Luna, …, A. Lostao. 2013. Detection of a quaternary organization into dimer of trimers of Corynebacterium ammoniagenes FAD synthetase at the single-molecule level and at the in cell level. *Biochim. Biophys. Acta.* 1834:665–676.
12. Nishi, H., K. Hashimoto, …, A. R. Panchenko. 2013. Evolutionary, physicochemical, and functional mechanisms of protein homooligomerization. *Prog. Mol. Biol. Transl. Sci.* 117:3–24.
13. Serrano, A., M. Sebastián, …, M. Medina. 2017. The trimer interface in the quaternary structure of the bifunctional prokaryotic FAD synthetase from Corynebacterium ammoniagenes. *Sci. Rep.* 7:404.
14. Serrano, A., S. Frago, …, M. Medina. 2013. Key residues at the riboflavin kinase catalytic site of the bifunctional riboflavin kinase/FMN adenylyltransferase from Corynebacterium ammoniagenes. *Cell Biochem. Biophys.* 65:57–68.
15. Cosconati, S., S. Forli, …, A. J. Olson. 2010. Virtual screening with AutoDock: theory and practice. *Expert Opin. Drug Discov.* 5:597–607.
16. Forli, S., and A. J. Olson. 2012. A force field with discrete displaceable waters and desolvation entropy for hydrated ligand docking. *J. Med. Chem.* 55:623–638.
17. Morris, G. M., R. Huey, …, A. J. Olson. 2009. AutoDock4 and AutoDockTools4: automated docking with selective receptor flexibility. *J. Comput. Chem.* 30:2785–2791.
18. Saridakis, V., D. Christendat, …, E. F. Pai. 2001. Insights into ligand binding and catalysis of a central step in NAD+ synthesis: structures of Methanobacterium thermoautotrophicum NMN adenylyltransferase complexes. *J. Biol. Chem.* 276:7225–7232.
19. Lee, J., X. Cheng, …, W. Im. 2016. CHARMM-GUI input generator for NAMD, GROMACS, AMBER, OpenMM, and CHARMM/OpenMM simulations using the CHARMM36 additive force field. *J. Chem. Theory Comput.* 12:405–413.
20. Jo, S., T. Kim, …, W. Im. 2008. CHARMM-GUI: a web-based graphical user interface for CHARMM. *J. Comput. Chem.* 29:1859–1865.
21. Olsson, M. H., C. R. Søndergaard, …, J. H. Jensen. 2011. PROPKA3: consistent treatment of internal and surface residues in empirical pK_a predictions. *J. Chem. Theory Comput.* 7:525–537.
22. Dolinsky, T. J., P. Czodrowski, …, N. A. Baker. 2007. PDB2PQR: expanding and upgrading automated preparation of biomolecular structures for molecular simulations. *Nucleic Acids Res.* 35:W522–W525.
23. Dolinsky, T. J., J. E. Nielsen, …, N. A. Baker. 2004. PDB2PQR: an automated pipeline for the setup of Poisson-Boltzmann electrostatics calculations. *Nucleic Acids Res.* 32:W665–W667.
24. Best, R. B., X. Zhu, …, A. D. Mackerell, Jr. 2012. Optimization of the additive CHARMM all-atom protein force field targeting improved sampling of the backbone φ, ψ and side-chain $\chi(_1)$ and $\chi(_2)$ dihedral angles. *J. Chem. Theory Comput.* 8:3257–3273.
25. Huang, J., and A. D. MacKerell, Jr. 2013. CHARMM36 all-atom additive protein force field: validation based on comparison to NMR data. *J. Comput. Chem.* 34:2135–2145.
26. Vanommeslaeghe, K., E. Hatcher, …, A. D. Mackerell, Jr. 2010. CHARMM general force field: a force field for drug-like molecules compatible with the CHARMM all-atom additive biological force fields. *J. Comput. Chem.* 31:671–690.
27. MacKerell, A. D., D. Bashford, …, M. Karplus. 1998. All-atom empirical potential for molecular modeling and dynamics studies of proteins. *J. Phys. Chem. B.* 102:3586–3616.
28. Pavelites, J. J., J. Gao, …, A. D. Mackerell. 1997. A molecular mechanics force field for NAD^+, NADH, and the pyrophosphate groups of nucleotides. *J. Comput. Chem.* 18:221–239.
29. Freddolino, P. L., K. H. Gardner, and K. Schulten. 2013. Signaling mechanisms of LOV domains: new insights from molecular dynamics studies. *Photochem. Photobiol. Sci.* 12:1158–1170.
30. Hess, B., H. Bekker, …, J. G. E. M. Fraaije. 1997. LINCS: a linear constraint solver for molecular simulations. *J. Comput. Chem.* 18:1463–1472.
31. Berendsen, H. J. C., D. van der Spoel, and R. van Drunen. 1995. GROMACS: a message-passing parallel molecular dynamics implementation. *Comput. Phys. Commun.* 91:43–56.
32. Abraham, M. J., T. Murtola, …, E. Lindahl. 2015. GROMACS: high performance molecular simulations through multi-level parallelism from laptops to supercomputers. *SoftwareX.* 1:19–25.
33. Frago, S., A. Velázquez-Campoy, and M. Medina. 2009. The puzzle of ligand binding to Corynebacterium ammoniagenes FAD synthetase. *J. Biol. Chem.* 284:6610–6619.
34. Serrano, A., S. Frago, …, M. Medina. 2012. Role of key residues at the flavin mononucleotide (FMN):adenylyltransferase catalytic site of the bifunctional riboflavin kinase/flavin adenine dinucleotide (FAD) Synthetase from Corynebacterium ammoniagenes. *Int. J. Mol. Sci.* 13:14492–14517.
35. Efimov, I., V. Kuusk, …, W. S. McIntire. 1998. Proposed steady-state kinetic mechanism for Corynebacterium ammoniagenes FAD synthetase produced by Escherichia coli. *Biochemistry.* 37:9716–9723.
36. Wang, W., R. Kim, …, S. H. Kim. 2005. Crystal structure of flavin binding to FAD synthetase of Thermotoga maritima. *Proteins.* 58:246–248.
37. Rao, S. T., F. Shaffie, …, M. Sundarlingam. 1992. Structure of the oxidized long-chain flavodoxin from Anabaena 7120 at 2 A resolution. *Protein Sci.* 1:1413–1427.
38. Hermoso, J. A., T. Mayoral, …, M. Medina. 2002. Mechanism of coenzyme recognition and binding revealed by crystal structure analysis of ferredoxin-$NADP^+$ reductase complexed with $NADP^+$. *J. Mol. Biol.* 319:1133–1142.
39. Lans, I., M. Medina, …, À. González-Lafont. 2012. Theoretical study of the mechanism of the hydride transfer between ferredoxin-$NADP^+$ reductase and $NADP^+$: the role of Tyr303. *J. Am. Chem. Soc.* 134:20544–20553.
40. Sebastián, M., A. Serrano, …, M. Medina. 2017. Kinetics and thermodynamics of the protein-ligand interactions in the riboflavin kinase activity of the FAD synthetase from Corynebacterium ammoniagenes. *Sci. Rep.* 7:7281.

Biophysical Journal, Volume *115*

Supplemental Information

The Dimer-of-Trimers Assembly Prevents Catalysis at the Transferase Site of Prokaryotic FAD Synthase

Isaias Lans, Juan Seco, Ana Serrano, Ricardo Burbano, Pilar Cossio, Martha C. Daza, and Milagros Medina

Supplemental information

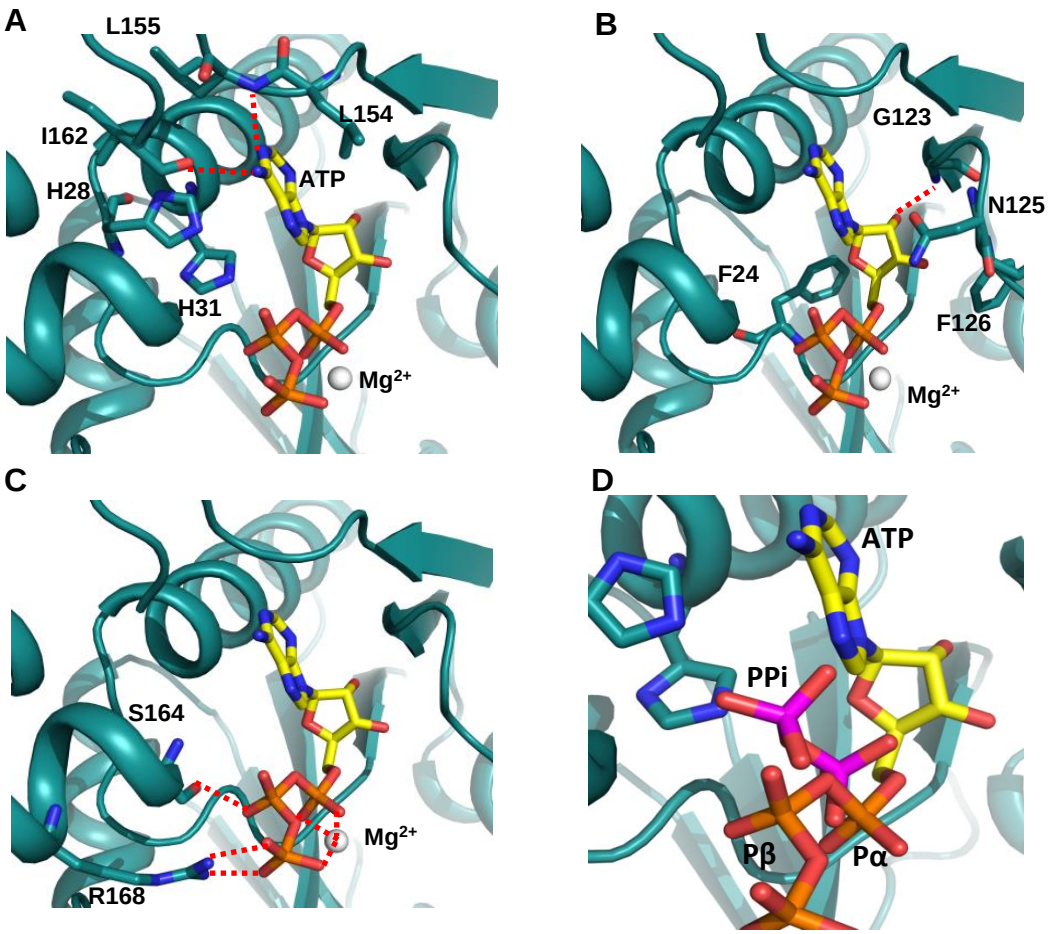

Figure S1. FMNAT:ATP/Mg^{2+} docking interaction model. (A) The adenine of ATP H-bonds to the L155 and I162 backbone atoms. (B) The ribose moiety of ATP H-bonds to G123 and its binding cavity is formed by the side-chains of F24, N125 and F126. (C) Mg^{2+} coordinates the ATP phosphates, while S164 and R168 stabilize the negative charges of Pβ and Pγ. (D) Superposition of the position of the PPi product (phosphates in magenta) in the crystallographic *Ca*FADS structure (2X0K) indicates that Pα and Pβ in the docking interaction model adopt an orientation close to that of PPi in 2X0K.

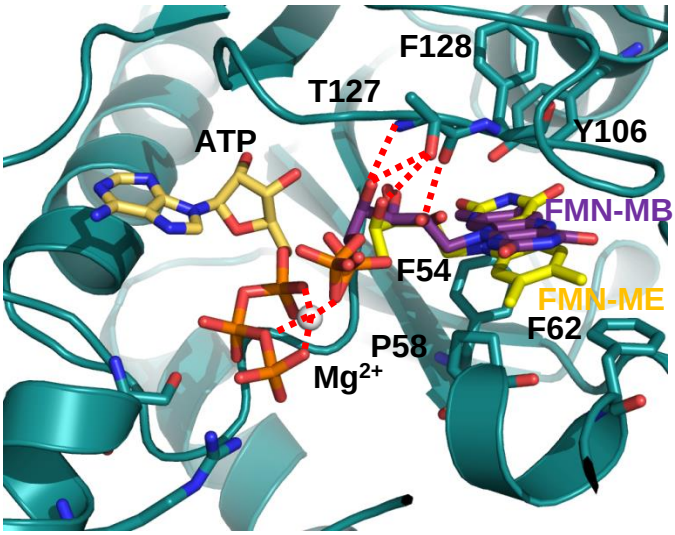

Figure S2. FMNAT:ATP/Mg^{2+}:FMN docking models. Best docking poses showing the two possible isoalloxazine ring orientations: methyls exposed to the solvent (FMN-ME, yellow) or buried inside the flavin binding pocket (FMN-MB, violet). In both, T127 stabilizes the position of the FMN ribityl chain, and Mg^{2+} is coordinated by FMN and ATP phosphates.

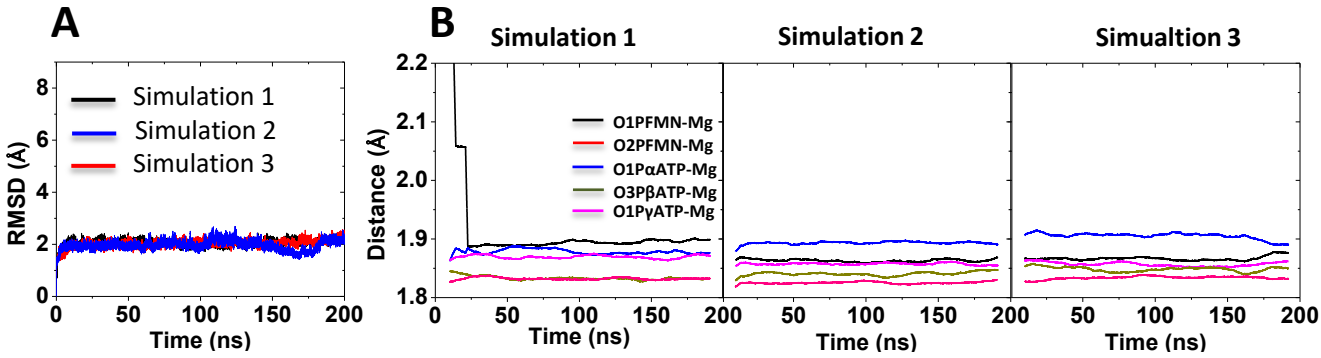

Figure S3. (A) Heavy atoms RMSD trajectories for the FMNAT:ATP/Mg^{2+}:FMN-ME (holo FMNAT) model along three MD replicas. RMSD values were calculated relative to the starting MD structure. (B) Time-window average (using a 20 ns window) distances of the Mg^{2+} atom to O1PFMN, O2PFMN, O1PαATP, O3PβATP, and O1PγATP (black, red, blue, green and magenta lines respectively) along the three MD replicas of the simulations.

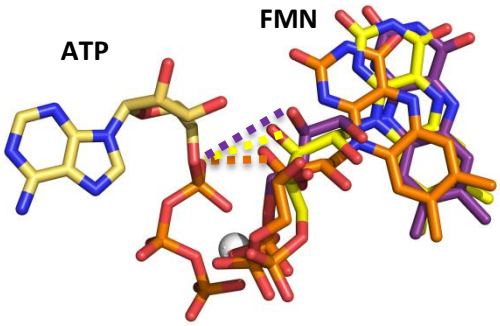

Figure S4. Ligand starting conformations for the holo FMNAT complex MD simulations. For simplicity only one ATP is showed. FMNs in orange and light yellow show shorter distances between its ribitiyl oxygens and ATP Pα Oxygens (doted lines).

Docking Model

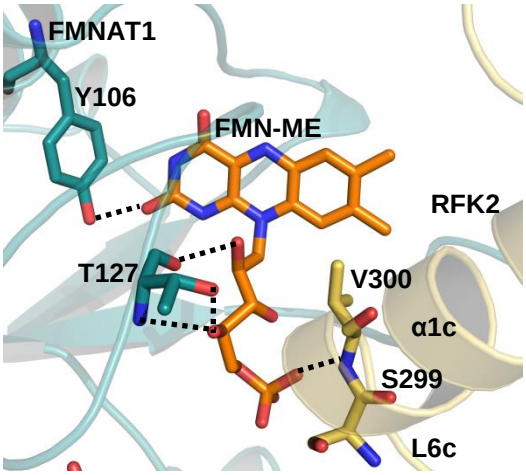

Figure S5. FMNAT:ATP/Mg^{2+}:FMN-ME:RFK (holo head-to-tail) docking model. The methyls of the FMN isoalloxazine point towards the neighboring RFK module (in yellow). T127 and Y106 at the FMNAT module (blue) contribute to the positions of the ribityl and the isoalloxazine ring the FMN. The FMN position is also modulated by V300 from the RFK module of the neighboring protomer.

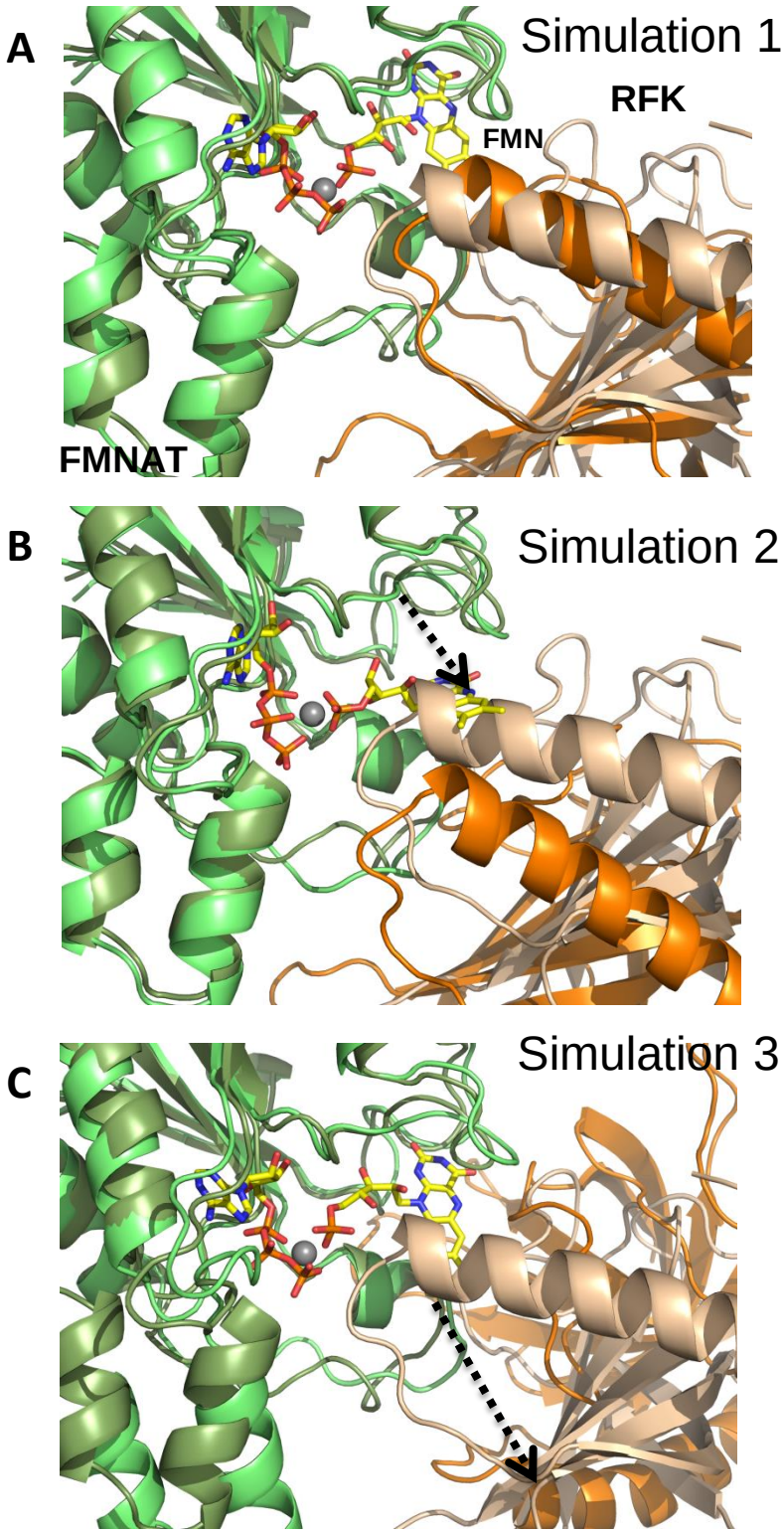

Figure S6. Comparison of the head-to-tail configuration from the apo *Ca*FADS crystallographic structure (FMNAT module in olive and RFK module in brown) with different snapshots of the holo head-to-tail model MD simulations (FMNAT in green and RFK module in Orange). Simulations show: (A) reorientation of the RFK module relative to the FMNAT one, (B) simultaneous reorientation of the RFK module and exit of the FMN flavin ring from its binding pocket (black arrow), and (C) semi-dissociation of the head-to-tail interaction (black arrow). These observations indicate that binding of substrates requires changes in the relative disposition of the RFK and FMNAT modules in the head-to-tail organization.

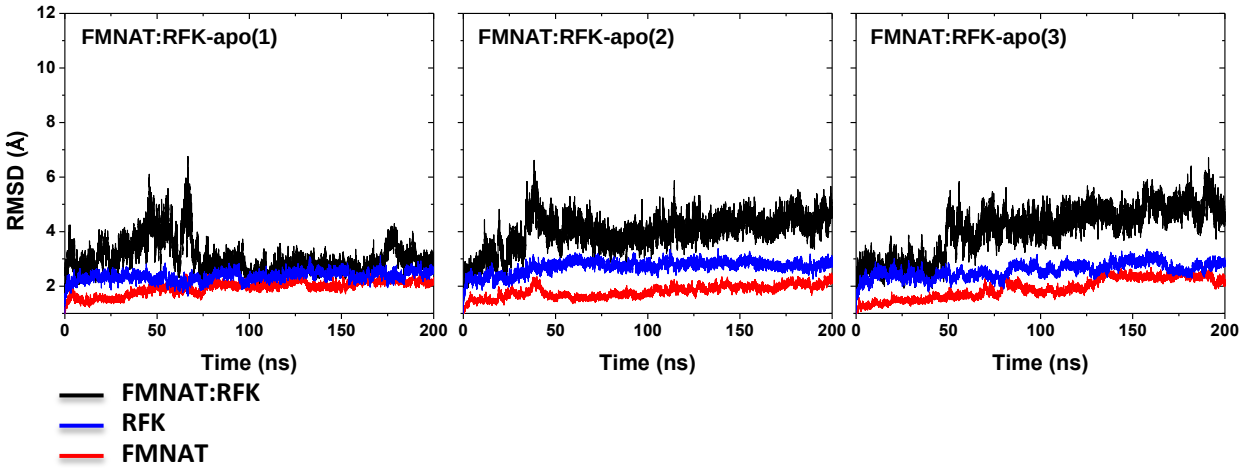

Figure S7. Relative disposition of the RFK and FMNAT modules along three MDs simulations replicas of the apo head-to-tail FMNAT:RFK model. Panels show evolution of the heavy atom RMSD trajectories when considering only the FMNAT (red line) or the RFK (blue line) modules, and the overall structure (black line). The RMSD values are calculated relative to the starting MD structure.

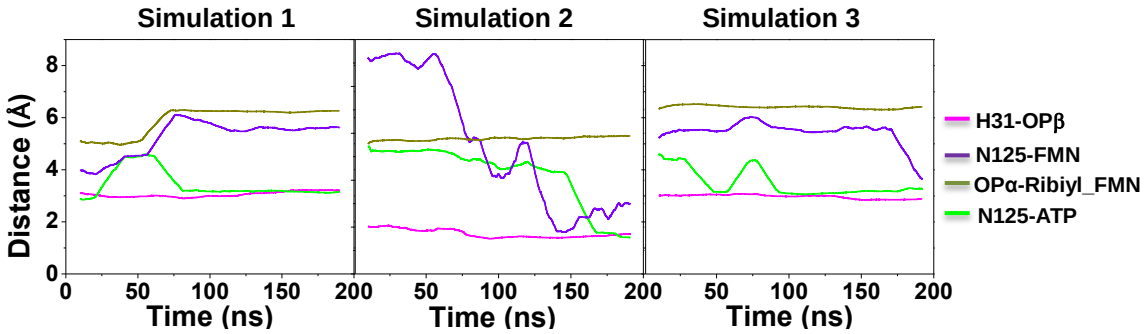

Figure S8. Trajectories of selected interaction distances along the three MD replicas of the holo head-to-tail model. The panels show the time-window average (using a 20 ns window) of the minimum distance between donor/acceptor pairs: H31-ATP, N125-ATP, N125-FMN and Pα oxygens-Ribityl of FMN (magenta, green, violet and olive respectively).

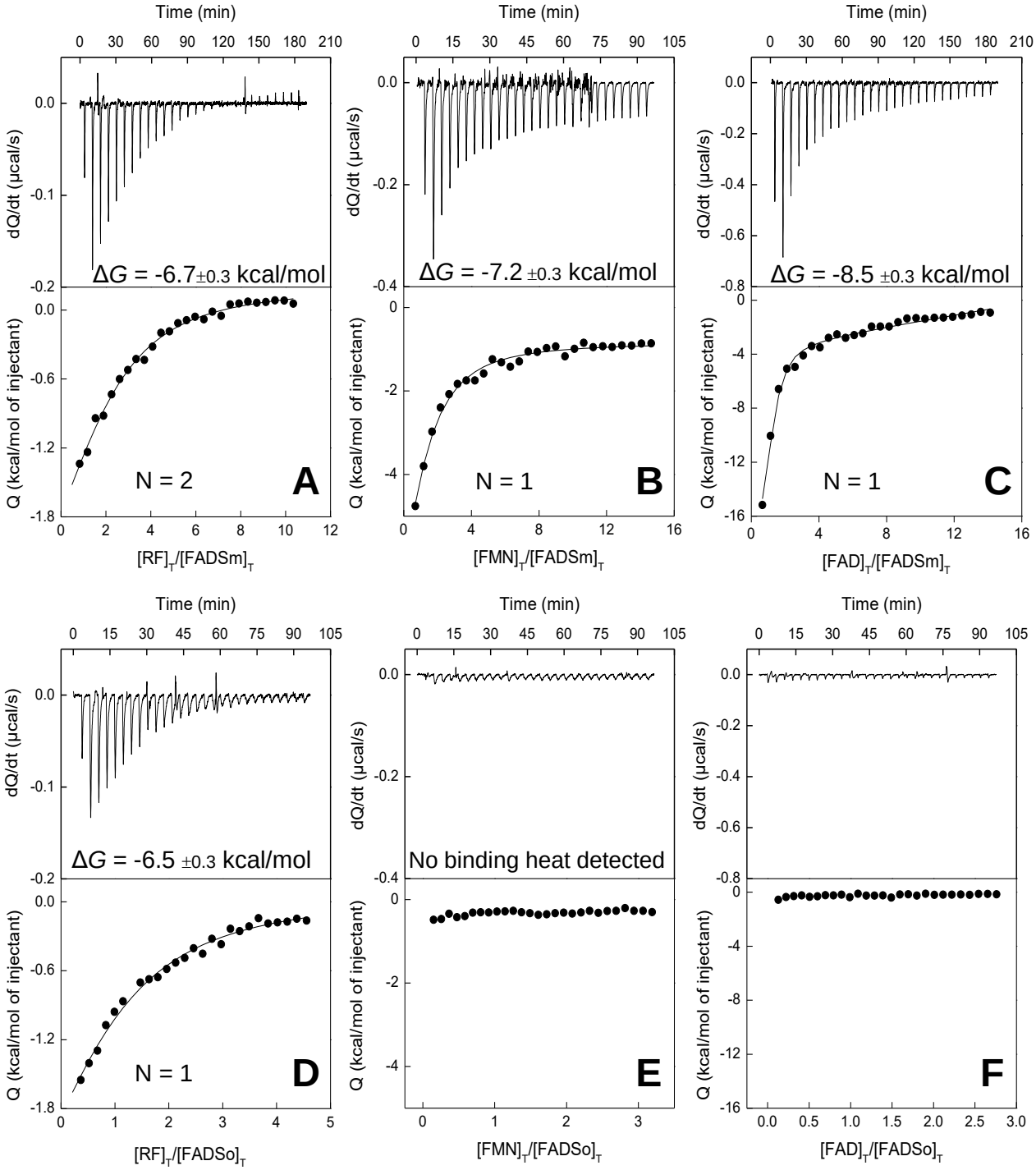

Figure S9. Calorimetric titrations of the ~100% FADS monomer (FADSm, top panels) and the ~100% FADS dimer-of-trimers (FADSo) with RF (A, D), FMN (B, E) and FAD (C, F). The upper panels show the thermograms for the interactions and the lower panels show the corresponding binding isotherms with integrated heats. Experiments were carried out in 20 mM PIPES, 10 mM $MgCl_2$, pH 7.0.